Communications Earth & Environment https://doi.org/10.1038/s43247-026-03182-y

Article in Press

Fiber-optic observations capture wind wave evolution in Lake Ontario

Received: 13 May 2025

Accepted: 2 January 2026

Cite this article as: Yang, C.-F., Spica, Z., Fujisaki-Manome, A. *et al.* Fiber-optic observations capture wind wave evolution in Lake Ontario. *Commun Earth Environ* (2026). https://doi.org/10.1038/s43247-026-03182-y

Chu-Fang Yang, Zack Spica, Ayumi Fujisaki-Manome & Yaolin Miao

Fiber-optic observations capture wind wave evolution in Lake Ontario

Chu-Fang Yang [1, *], Zack Spica [1], Ayumi Fujisaki-Manome [2, 3], Yaolin Miao [1]

[1] Department of Earth and Environmental Sciences, University of Michigan, Ann Arbor, MI, USA

[2] Cooperative Institute for Great Lakes Research (CIGLR), University of Michigan, Ann Arbor, MI, USA

[3] Department of Climate and Space Sciences and Engineering, University of Michigan, Ann Arbor, MI, USA

Correspondence to Chu-Fang Yang (chufan@umich.edu)

* Now at Université Côte d'Azur, CNRS, Observatoire de la Côte d'Azur, IRD, Géoazur, Valbonne, France (kim.yang@geoazur.unice.fr)

Key points:

1. Fiber-optic observations show that chaotic waves, which generate high-frequency microseisms, can evolve into wind waves, which produce low-frequency microseisms.
2. Dominant frequency of low-frequency microseisms depends on wind speed and fetch.
3. Peak frequency variations of low-frequency microseisms can track wind wave evolution.

Abstract

Storm-induced waves threaten ship traffic and offshore infrastructures, yet observing water surfaces remains challenging because of complex air-water interactions and limited spatial coverage. We used distributed acoustic sensing measurements from a telecom fiber-optic cable in Lake Ontario, one of the world's largest lakes, to analyze wind-wave evolution at tens-of-meter scales along a 43-km-long array. By combining observations and modeling, we found that chaotic waves induced by local wind forcing and wave-wave interactions generate high-frequency microseisms (1-4 Hz), whereas frequency variations in low-frequency microseisms (0.2-1 Hz) are strongly controlled by wind speed and fetch evolution. We tracked changes in frequency and energy throughout the full life cycle of wind waves, from chaotic conditions to organized gravity waves formed under steady winds, followed by dissipation as fetch decreases. These results are particularly relevant for fetch-limited water bodies and highlight the potential of distributed acoustic sensing for real-time monitoring of wind waves, with implications for coastal hazards, ecosystem dynamics, and wave-energy development.

Keywords: Distributed Acoustic Sensing, Great Lakes, microseism, wind wave, wind fetch

1. Introduction

Storm-induced rogue waves are among the most impactful natural hazards and are being increasingly observed in coastal oceans and large lakes [1]. Their increasing occurrence may be linked to climate change, raising concerns about their potential impacts [2]. Such destructive waves evolve from wind waves through a series of dynamic interactions between the atmospheric boundary layer and the water surface, transferring energy and momentum from wind to waves. As wind blows over water, wind stress creates ripples and capillary waves [3, 4, 5], which can grow in wavelength and amplitude under persistent stress forcing as gravity becomes the dominant restoring force [6, 7], leading to the formation of surface gravity waves. These wind-driven surface gravity waves (hereafter 'wind waves') are strongly influenced by the local wind conditions. They gain energy from the wind and redistribute it within the wave spectrum through nonlinear wave-wave interactions (e.g., four-wave resonant interactions), resulting in a downshift of the dominant spectral energy toward lower frequencies and longer wavelengths [8]. With sufficient wind speed, duration, and fetch, the wave trains evolve into swells that can propagate thousands of kilometers from their generation area without strong wind forcing [9]. At this stage, the swells no longer gain energy from local winds but lose it to the atmosphere [10]. Wind wave evolution is a complex air-water interacting process, involving a broad range of scales, from seconds to hours in time and from millimeters to kilometers in space.

In addition to the interactions at the air-water interface, wind wave-induced pressure perturbations can excite ground motions on the Earth's surface. Modern geophysical instruments, such as seismometers, geophones, and hydrophones, can detect microseisms induced by wind-driven waves on the ocean and lake surface (e.g., refs. [11, 12]). Ocean surface waves directly couple with shallow-water seafloor topography and induce low-frequency microseisms (LFMs, typically observed ranging from 0.085 to 0.2 Hz), known as primary microseisms [13, 14]. The LFM energy correlates with changes in seafloor pressure caused by variations in wind field and wave height [15, 16]. It can be used to track distant storms, which are typically associated with large waves (e.g., ref. [17, 18]), and to estimate storm intensity [19]. Furthermore, the ocean surface waves interacting with opposite-direction waves and reflective waves from coasts generate high-frequency microseisms (HFMs, typically observed ranging from 0.2 to 0.45 Hz), known as secondary microseisms [13, 20, 21]. The HFMs primarily consist of seismic surface waves, particularly Rayleigh waves [22, 23]. Their frequencies vary depending on local ocean conditions, topography, and subsurface geological structures [24, 25]. Besides, nonlinear ocean wave-wave interactions can generate HFMs at approximately double the frequency of the original waves [26]. Similarly, lake-generated microseisms have been observed in large lakes, such as Yellowstone Lake [27, 28], the Great Lakes [29, 30], the Great Slave Lake [31 32], and Lake Malawi [33]. Like ocean microseisms, microseisms in lakes are induced by the wind-driven waves and exhibit both HFMs and LFMs, but with a higher range of 0.2-2 Hz due to the lakes' smaller size [27, 33, 34]. Such microseisms are influenced by factors like lake shape alignment with wind direction and diurnal wind changes in lake environments [27, 33]. Since the microseisms are a part of the energy transition from wind-driven waves to seismic waves, the microseism spectrum can offer insights into the complex dynamics between wind, waves, and lake environments [34].

Wind wave spectrum provides practical information for understanding the wave dynamics and their interactions with atmospheric, oceanographic, and coastal processes. Pierson and Moskowitz [35] proposed the first simple wind-wave spectrum (i.e., the Pierson-Moskowitz spectrum) for fully developed seas where waves achieve their maximum size under constant wind. The empirical relationship of the wave spectrum describes the energy distribution of the waves as a function of wave frequency and the peak frequency of energy as a function of wind speed. However, Hasselmann et al. [36] found that the waves never fully develop and may continue to develop through nonlinear wave-wave interactions during the Joint North Sea Wave Observation Project (JONSWAP). The JONSWAP spectrum defines a modified empirical relationship based on the Pierson-Moskowitz spectrum, accounting for the energy supplied by increasing wave distance and incorporating a factor that enhances the peak energy. Shapes and amplitudes of the spectrum are attributed to wave periods and energy, reflecting the relationship between wind speed, fetch, and duration. Temporal variation of the spectrum implicates how waves evolve with changes in wind conditions and interact with others. Due to instrumental limitations, the wave spectrums have been primarily documented through single-station measurements using buoys, pressure sensors, or wave gauges (e.g., ref. [37, 38]). Dense arrayed observations are required to better understand the finer details of wind wave evolution.

Distributed acoustic sensing (DAS) is an emerging technology that converts optic-fiber cables into dense, high-resolution seismic arrays spanning approximately a hundred kilometers. DAS uses optical backscattering from a single power source to measure absolute strain along the fiber, significantly increasing the spatial and temporal resolution of seismic data to a few meters and hundreds (or thousands) of hertz. Furthermore, existing subsea telecommunication fiber-optic cables can be converted into vast observational networks for exploring our planet's inner space—the ocean. Previous studies have shown that subsea DAS arrays can detect insightful microseisms and hydrodynamic processes associated with ocean surface waves [39, 40], tsunami waves [41], ocean currents [42, 43, 44], and internal waves [45]. Xiao et al. [46] used DAS data to locate the precise sources of HFMs, which were found to align with the incoming wind patterns. In addition, DAS arrays have been used to derive HFM dispersion relationships, which can then be applied to image offshore subsurface structures [47]. These studies demonstrate the potential of the DAS technique for advancing marine geophysics and physical oceanography.

Converting DAS signals to physical parameters is critical for future monitoring applications. Meulé et al. [48] studied the relationship between wind-wave-generated seabed strains from a DAS array and pressure fluctuations from a co-located pressure sensor. They successfully established a transfer function to convert the cable deformation to significant wave height. However, the DAS-detected wave-generated strains are affected not only by source motions (e.g., wave movements and their complex interactions) but also by local properties [48, 49, 50, 51] (e.g., water depths, seafloor topography, geological structure, and/or cable coupling with the seafloor). The exact mechanisms of how the stresses are transferred from water to the optic-fiber cable still need additional studies using DAS in different configurations and environments [48]. In addition to local effects, how microseism energy and frequency vary with wind wave development has not been thoroughly investigated, making it difficult to systematically utilize the microseisms to monitor the wave states.

To characterize wind wave evolution in a confined water environment, we used DAS data collected from a telecommunication fiber-optic cable deployed along the bottom of western Lake Ontario, one of the world’s largest lakes that resembles coastal oceans in its physical processes (Fig. 1a). The DAS measurements were taken along this cable, known as the Crosslake cable (hereafter referred to as the 'Crosslake DAS array'), between May 2023 and March 2024. This was the first and largest DAS array measured in the Great Lakes. The Crosslake DAS array has nearly 5000 channels with 10 m spacing in 50 km, measuring the strain variation along the cable from Toronto. The underwater segment of the array is located at water depths ranging from 0 to

~140 m, approximately 43 km long, starting from channel 700 to the end of the array channel (Fig. 1b, c). Lake Ontario has a maximum depth of 244 m and an average depth of 86 m, which can support wind-generated waves with wavelengths ranging from a few tens to a few hundred meters. Most areas of the lake can thus be considered effectively deep water [9, 35, 36], which corresponds to the JONSWAP model's deep-water assumption.

In this study, we applied wave spectrum concepts to investigate the generative mechanisms of microseisms, characterize the spatiotemporal variability of wind waves in the lake, and illustrate how high-frequency chaotic waves progressively evolved into coherent low-frequency wind waves using DAS data. Real-time, high-spatiotemporal DAS observations, which use lake-bottom telecommunication cables that are less likely to be damaged by surface destructive waves, may help detect rapid wind-wave changes (on the scale of minutes) and improve the safety of lake-state monitoring during severe winter weather.

2. Results

2.1 Data overview

To examine if the DAS is able to characterize wind-wave-induced microseisms, we select two 36-h recordings with different wind speeds according to on-site observations at Station Olcott, located on the south shore of Lake Ontario: a moderate wind event from 12 UTC on May 16 to 00 UTC on May 18, 2023, and a winter storm event from 12 UTC on January 9 to 00 UTC on January 11, 2024, with near-surface wind speeds of 5-10 m s^{-1} and 10-20 m s^{-1}, respectively. Winter storms are generally associated with continuous, strong winds and variable gusts, leading to diverse wave dynamics. The coexisting waves arising from these different dynamics can simultaneously grow, reflect, interfere, and dissipate within the lake, resulting in complex wind-wave and wave-wave interactions. In contrast, moderate winds are associated with fewer interactions and result in more distinguishable wave systems, which help clarify how waves develop under stable wind conditions.

The Crosslake DAS array detected distinct wind-wave-induced microseisms between 0.2 and 4 Hz in both events. The HFMs have an approximately fixed frequency of 1.3 Hz, continuously detected at the array center (Fig. 2a, c). In contrast, the LFMs show varying frequencies, with peak frequencies changing between 0.2 and 1 Hz over time (Fig. 2a, c). The dominant frequency band of microseisms in Lake Ontario is generally consistent with that observed in other lake environments [27, 28, 29, 30, 31], but higher than that typically reported in oceanic environments [13, 14, 20, 21]. This frequency difference is governed by the distance wind blows across the water surface (fetch) [34]. Although this distance is presumably constrained by the lake's modest size, it has not been systematically studied. In the time domain (Fig. 2b, d), higher amplitudes of the microseisms closely correspond to the timing of the changing of wind speed and directions observed at Station Olcott. The microseisms propagate toward the southeast at an apparent speed of ~3 m s^{-1} when the averaged wind direction changes from southwesterly to northwesterly in the moderate wind event (Fig. 2b). Although the winter storm induces complex wave states in the lake, the strong microseisms can still be distinguished propagating toward the northeast at an apparent speed of ~10 m s^{-1} when the wind changes from southeasterly to southwesterly (Fig. 2d).

The multi-channel spectra (Fig. 3) show that the DAS data's energy peaks are primarily in the frequency bands of microseisms between 0.2 and 4 Hz and that of infragravity waves between 0.02 and 0.1 Hz. Among them, the HFMs between 1 and 4 Hz are the most energetic and have the highest power spectral densities (PSDs), particularly near the center, deeper segment of the array. The peak frequency increases as the water depth gets shallower toward the north and south slopes, respectively, while the energy decreases as the channel of the cable approaches the lakeshore (Supplementary Fig. 1). The frequency changing along the cable shows a similar pattern in both events, indicating that the dominant frequency is governed by local factors such as water depths and subsurface structures. The spectral energy of the LFMs between 0.2 and 1 Hz extends from the HFM energy, suggesting that both microseisms originate from the same source. The LFM peak frequency in the winter storm event (Fig. 3b) extends to a lower frequency at 0.35 Hz than that in the moderate wind event (Fig. 3a), approximately at 0.45 and 0.6 Hz. Furthermore, the PSDs of the winter storm event are greater than those in the moderate wind event, demonstrating that microseism energy is primarily related to the wind speed. In terms of spatial distribution, the stronger microseisms in both events are found near the deepest segment of the cable, farther away (20-25 km) from the shore.

The HFMs, LFMs, and infragravity waves are produced by different mechanisms of wind-wave-dynamic processes. The infragravity waves of 0.02-0.1 Hz are generated through the interaction and grouping of wind-driven waves. These waves propagate as longer-period gravity waves, following the gravity wave dispersion curve $\omega^2 = gk \cdot tanh(kh)$ in the frequency-wavenumber domain (Supplementary Fig. 2). The ω is angular frequency, g is gravitational acceleration, k is angular wavenumber, and h is water depth. The HFMs and LFMs involve the transition of energy from wind waves to seismic waves and propagate as seismic body waves or surface waves in solid Earth. Their dispersion relationship depends on the elastic properties of the sub-bottom structures. Here, we focus on spatiotemporal variations of two microseismic frequencies (i.e., HFM and LFM) in Lake Ontario and study their evolutions attributed to wave dynamics, wind-wave developments, and interactions.

2.2 High-frequency microseisms

Coupling of pressure perturbation from wind- and wave-wave interactions with the lake floor generates the HFMs [13, 20]. Under weak wind conditions (<5 m s^{-1}; Supplementary Fig. 3), the energy associated with the wind field is relatively low. In the frequency-phase-velocity domain (Supplementary Fig. 2), the HFMs have a fundamental mode at ~1 Hz, with additional modes at higher frequencies, and the phase velocities disperse dramatically over a few hertz. These features show that the HFMs are rapidly dissipated seismic surface waves. To better understand how wind waves influence spatiotemporal variations in HFMs, we compare these variations with the spatiotemporal variability of wind field (hereafter 'wind variability'; see 'Methods'). This wind variability is estimated from the National Weather Service's National Digital Forecast Database (NDFD), which serves as the forcing dataset for the Great Lakes Operational Wave Model based on WAVEWATCH III (WW3) [52, 53, 54, 55]. Although the NDFD and WW3 data are analyses and simulations respectively rather than field measurements, they provide a first-order approximation for both spatial and temporal variations of wind and wave in Lake Ontario. Since waves are modulated by wind conditions accumulated over a certain time frame instead of instantaneously, the time difference of the wind field, which quantifies changes in wind speed and direction over time, can be considered to represent the energetics of wind-wave interactions. Wind-wave interactions involve complex relationships between the wind blowing over the water surface and the waves it generates. Variations in wind speed and direction directly affect the size, shape, and propagation of the waves. The wind variability can thus be utilized to study wind-wave interactions as sources of HFMs.

The high energy of HFMs in both moderate wind and winter storm events is mostly associated with significant wind variability (>4 m s^{-1}) as the wind field changes in its direction. During the moderate wind event, the high-energy HFMs gradually shift southward between May

16, 21 UTC and May 17, 00 UTC (Fig. 4b), while an east-west wavefront pushes an area of inconsistent wind-wave directions southward under the influence of north-northwesterly winds between May 16, 23 UTC and May 17, 01 UTC (Fig. 4a). In addition to the NDFD's wind variability estimates, significant wind variability is also observed at Station Olcott around 01 UTC on May 17, occurring about three hours later than at the array's center segment. The higher water levels at the same time are most likely caused by the interactions between incoming waves from the north and waves reflected off the shore. During the winter storm event (Fig. 4d), the high energy of HFMs correlates to high water levels at Olcott between 00 and 02 UTC on January 10 and significant wind variability between 03 and 05 UTC on January 10. The center segment of the array (channels 2435-3235) detects the most energetic HFMs around 04 UTC, while another east-west wavefront propels an area with a pronounced difference in the wind-wave directions northward by southerly winds (Fig. 4c). Both events show that the downstream of the wavefronts has a considerable wind variability zone, which forms the area with high energetics of breaking (chaotic) waves caused by incoherent wind-wave propagation (gray shading in Fig. 4a, c).

The NDFD and WW3 data (Fig. 4a, c) depict the wind-wave front movements that are spatiotemporally consistent with the propagation of prominent microseisms recorded by the DAS array (Fig. 2b, d). The high-amplitude microseisms in the moderate wind event (Fig. 2b) present an apparent speed of ~3 m s^{-1} propagating southeast along the DAS array. Such speed is much slower than the typical phase velocity of seismic surface waves, which ranges from hundreds to thousands of meters per second. Instead, the speed matches the wind velocity, suggesting that the HFMs are seismic waves induced by the wind-driven chaotic waves at the water surface, resulting from wind-wave interactions. The complex wind- and wave-wave interactions are difficult to predict, and the hourly NDFD and WW3 data may lack spatiotemporal resolution to capture such small-scale and short-period chaotic waves. The inconsistent variations may also be caused by interactions with shoreline-reflected waves and swells, which are typical during storm events. Unlike locally generated waves, they are less affected by wind variability and thus more difficult to characterize. As a result, the NDFD wind variability does not precisely fit the HFM energy variations. However, the high energy of HFMs generally matches the region where the significant wind variability passes through the array.

2.3 Low-frequency microseisms

To examine if the DAS-detected LFM variations are related to the wind waves in the lake, we treat the LFM spectrum as the JONSWAP wave spectrum to characterize wave features based on the empirical functions of the JONSWAP spectrum. According to the JONSWAP spectrum [36] (see 'Methods'), the peak frequency of wave spectral density, $f_p = \frac{22}{2\pi}\left(\frac{g^2}{U_{10} \cdot F}\right)^{\frac{1}{3}}$, corresponding to the dominant wave period (Supplementary Fig. 4), is a function of gravitational acceleration (g), wind speed at 10 m above the surface (U_{10}), and wind fetch (F). The wind fetch refers to the uninterrupted distance over water that the wind travels without changing its blowing direction or encountering major obstacles (e.g., land or another wave system from a different direction). Essentially, the farther the wind blows over a distance, the larger and more powerful the waves it can generate, as it has more time and space to transfer energy to the water. As a result, the wind fetch helps define the potential of wave growth and development, including changes in wave height and periods. Although wind fetch cannot be directly measured, and the observational wind speed co-located with the DAS array is unknown, we can estimate $U_{10} \times F = g^2\left(\frac{22}{2\pi f_p}\right)^3$ using the primary peak frequency identified in the multi-channel LFM spectrum every 10 min of the DAS data. The peak frequency has an inverse exponential relationship with the $U_{10} \times F$. The decrease in frequency indicates wave development into a longer period, while the increase in frequency signifies wave dissipation into a short period. Thus, we define the DAS-estimated $U_{10} \times F$ as the 'empirical wave growth factor' (hereafter 'empirical wave factor'; see 'Methods') and analyze its spatial and temporal variations in comparison to the NDFD wind and WW3 wave data.

The pronounced variations in the empirical wave factors (Fig. 5b, f), such as those observed around May 16 at 21 UTC and January 10 at 06 UTC, are generally associated with transitions in WW3 significant wave height from high to low values (Fig. 5a, e). In the moderate wind event, the variations of empirical wave factor (Fig. 5b) and LFM peak-frequency energy (Fig. 5c) show that a prominent wind wave is propagating toward the south shore at an apparent speed of ~3 m s^{-1} between 21 and 23 UTC on May 16. This wave progressively develops behind the wavefront, where the wind and wave move in the same direction (Fig. 4a). Around 00 UTC on May 17 (Fig. 5c), the wind wave is reflected by the south shoreline, heading north at a similar speed. The reflected waves exhibit reduced LFM energy (~25 dB; Fig. 5c) but an increased wave factor (~2.5×10^4 m^2 s^{-1}; Fig. 5b). This suggests that, due to nonlinear interactions between incoming and reflecting waves, the wave period may increase while the wave height decreases. As the northerly wind (Fig. 5a) continues to blow from 06 to 18 UTC on May 17, waves with high energy of HFMs propagate toward the south shore (Fig. 5d). In the following hours, these waves are accompanied by increases in LFM energy and wave factors (Fig. 5b, c). However, the WW3 model underestimates these high waves (Fig. 5a). In contrast, the winter storm event shows insignificant reflected wave patterns but a distinct wave generation process. Before the wind direction changes from easterly to southerly around 05 UTC on January 10 (Fig. 5e), the

DAS array detects high wave factors (~1.5×10^5 m^2 s^{-1}) associated with lower LFM energy (Fig. 5f, g), showing that the dominant waves (swells) come from the east but are dissipating. After the wind direction changes to southerly and further to westerly, a new wave starts to develop associated with the increasing wave factors and propagates toward the north shore. While the wave develops to ~10^5 m^2 s^{-1} between 06 and 15 UTC on the same day, the array detects strong LFM energy of ~40 dB near the center segment of the array. Both the LFM energy and the empirical wave factors start to diminish around 15 UTC, indicating that the wave is dissipating.

Both events are similar in that the integral HFM energy has higher amplitudes before the wind wave starts to form (Fig. 5d, h), while the LFM energy gradually increases as the wave grows (Fig. 5c, g), such as the periods from 22 to 23 UTC on May 16, from 07 to 18 UTC on May 17, and from 18 UTC on January 10 to 18 UTC on January 11. The high energy of HFM is followed by the increase of LFM energy implies a potential mechanism in which the energy of high-frequency chaotic waves is accumulated through continuous, consistent winds and subsequently transferred to low-frequency waves. Besides, the empirical wave factors are closely related to the wind condition. The wave factor varies dramatically when the wind direction changes, e.g., on May 16, from 21 to 22 UTC, and on January 10, from 04 to 05 UTC. The increase in the empirical wave factor implies that the wave is formed due to an increase in wind speed, wind fetch, or both influences, and that its wavelength and period extend. However, the high wind speed and wave factor do not occur concurrently between January 9, 18 UTC, and January 10, 05 UTC (Fig. 5e, f). As a result, in addition to wind speed, wind fetch developments may have a substantial impact on wave growth and period.

2.4 Influence of wind fetch on low-frequency microseisms

To examine how wind speed and wind fetch affect the LFMs, we compare the time series of the empirical wave factor and LFM energy with those of the NDFD wind field, WW3 significant wave height, and the estimated wind fetch and wave growth factor. The estimated wind fetch is calculated using the definition of effective fetch (F_e) from the Shore Protection Manual [56] (see 'Methods'). To obtain the wave growth factor, we multiply the effective fetch (F_e) by the height-corrected NDFD wind speed (U_{10}; see 'Methods'), define it as the 'theoretical wave growth factor' ($U_{10} \times F_e$; hereafter 'theoretical wave factor'), and present its time series at the array center for the entire month of January. During this period, there were two major winter storms passing Lake Ontario between January 9 and 15.

Fig. 6a shows that the theoretical wave factor variations strongly correlate with the wind fetch variations. The local maxima of wind fetch (>100 km) and theoretical wave factor (>2×10^6 m^2 s^{-1}), such as those on January 7, 10, 13, and between 24 and 29, correspond to the persistent easterly wind blowing over Lake Ontario. When the winds change to westerly, the fetch and wave factor mostly reduce to less than 100 km and 2×10^6 m^2 s^{-1}, respectively. In addition, despite constant, strong westerly winds (>15 m s^{-1}) during the storm period, the corresponding wave factors are still low (<2×10^6 m^2 s^{-1}). Such wind direction-dependent phenomena are related to the pronounced difference in the distances of the DAS array to the west shoreline (<85 km) and to the east shoreline (~250 km), resulting in the distinct growth spaces for the westerly and easterly waves. Therefore, compared to the influence of wind speed, variations in wind fetch caused by changes in wind direction across Lake Ontario have a stronger influence on wave growth and dominant wave period, which in turn controls the LFM peak frequency.

The variations in theoretical and empirical wave factors virtually correlate with each other (Fig. 6a). Averaging the empirical wave factors hourly and correcting those time shifts with the theoretical wave factors every 5-6 days reveals a strong correlation between the two datasets. Although the empirical wave factors are underestimated by an order of magnitude compared to the theoretical wave factors, the linear regression shows correlation coefficients of R=0.76 for the storm period (Fig. 6b) and R=0.72 for the entire month of January (Fig. 6c), with confidence levels of ±0.03 and ±0.02, respectively. In contrast to the empirical wave factors, the LFM energy variations are more similar to the wind speed and significant wave height variations (Fig. 6a). Particularly during the storm period, the LFMs induced by the westerly waves with increased energy correspond to higher wind speeds and wave heights, while those induced by the easterly waves are associated with lower peak frequencies and lower energy, indicating that the waves may be swells propagating over longer distances but at lower heights. The results demonstrate that, for deep water regions, both wind speed and wind fetch are crucial factors in controlling the size and growth of waves [3, 36], as well as in the dissipation of wave energy, especially once the transmission of wave energy reduces due to decreases in wind speed or changes in wind direction. This mechanism leads to a frequency-dependent (or wave period-controlled) process [57], as evidenced by the variations of empirical wave factors and LFM peak frequencies. Although buoys can observe wave periods in situ, they are removed from the Great Lakes during the winter. However, the DAS array, which functions similarly to a dense buoy array, can detect high-resolution spatiotemporal variations in LFM frequency and characterize wave development and dissipation. This capability makes it a valuable tool for monitoring wave states in lakes with the deep-water conditions.

3. Discussions

The DAS array in Lake Ontario observes spatial- and temporal-dependent frequency changes in the HFMs and the LFMs, respectively. The phase velocity of HFMs as a function of frequency (Supplementary Fig. 2) demonstrates the dispersion characteristics of seismic surface wave energy and its multiple overtones, indicating that the HFMs are Scholte waves propagating at the fluid-solid earth interface [46]. The Scholte waves are induced by ground motions generated by the extra pressure from the chaotic waves on the water surface, which forces the lake floor. Their frequencies are mostly influenced by water depth, local topography, and subsurface structure, and their energy decays rapidly. The observed apparent speed of microseisms from strain time series is much slower than their phase velocity estimated from frequency-wavenumber analysis, suggesting that the HFMs are generated by multiple moving sources caused by varied wind fields disturbing the surface of the lake. Such wind-wave interactions can rapidly generate high-frequency chaotic waves, including ripples in the early stage of wave formation and wind-driven wave breaking, which induce HFMs. Additionally, interactions between directly generated waves and reflected waves from the shorelines (i.e., wave-wave interactions) can also generate HFMs. These chaotic waves, created through both mechanisms, are ubiquitous across the water surface. Consequently, continuous HFM signals can be observed in the seismic spectrograms (Fig. 2a, c).

The peak frequency of LFMs corresponds to the dominant wave period in the spectrum. The frequency variations over time illustrate the growth and dissipation of this dominant wave. However, we observe multiple LFM peak frequencies in the spectrum, indicating the simultaneous presence of numerous wave sources. These sources are influenced by wind direction changes and the reconstruction of fetch due to the growing waves. For instance, double-frequency periods are evident from 06 to 18 UTC on May 17 and from 05 to 07 UTC on January 10, as shown in the spectrograms (Fig. 2a, c). Furthermore, we observe that the timing of high empirical wave factors does not coincide with the peak-frequency energy during the winter storm event. This suggests that the long-period waves have traveled a considerable distance along the previous wind direction and are gradually fading. By combining information about the LFM peak frequency with energy variations in the DAS spectrum, we can reconstruct the wave patterns in large lakes and even in oceans.

The presence of strong microseisms, both HFMs and LFMs, near the center segment of the array may be related to the wave development and fewer interactions with shoreline topography. When wind blows across the surface of water, it transfers energy to the water and creates waves. As long as the wind continues to blow in the same direction, a longer fetch allows waves to accumulate more energy, enabling them to grow larger, associated with a rise in wave height and period over time. As the waves approach shallow water areas near the shoreline, they may lose energy due to friction with the lake floor, resulting in wave breaking and turbulence. Therefore, there is a greater chance of the high-energy, mature waves occurring closer to the center of the array, away from the shores. In addition, the interaction of waves with the wind and other waves can thus result in greater energy of chaotic waves near the array center while the energy dissipates toward the north and south shorelines, respectively.

Based on the observed energy decay and growth between HFM and LFM, consistent wind conditions may accumulate energy from chaotic waves and subsequently transfer it to enhance wind-wave amplitude as the fetch increases. During both moderate wind and winter storm events, our observations indicate that the high-energy HFMs are followed by increases in LFM energy. The LFM energy increases as its dominant frequency decreases from the HFM frequency of 1.3 Hz. The NDFD data (Fig. 4a, c) depict that the high-frequency chaotic waves generated by wind-wave interactions are predominantly distributed ahead of the wavefront. As the wind carries the wave onward, the developing wave acquires energy from wind and organizes these chaotic waves (and ripples), resulting in growth behind the wavefront while the wave's frequency decreases (Fig. 7). These findings present a different perspective on the causal relationship between the evolution of primary and secondary microseisms. Traditionally, ocean surface waves, which are sources of LFMs (or primary microseisms), can produce chaotic waves, which are sources of HFMs (or secondary microseisms), by nonlinear interactions with other waves [14]. In this dynamic process, the secondary microseisms are generated after the primary microseisms. However, our findings suggest an alternative possibility: continuous wind action on the water surface can induce HFM through ripples formed at the early stage of wind-wave development. In other words, secondary microseisms do not necessarily follow primary microseisms and may, in some cases, precede them.

Microseisms observed in Lake Ontario present a frequency band of 0.2-4 Hz, which is higher than the typical range observed in oceanic environments (0.085-0.45 Hz) [12]. Wind speed and wind fetch, with the effective fetch determined by the water surface distance along the wind direction, are crucial factors in defining the frequency bands of microseisms. Under consistent wind conditions, the lower-bound frequency of LFMs is constrained by the spatial extent and boundaries of the water body; the larger the water surface area, the lower the frequency of LFMs. For example, Lake Ontario’s east-west elongated elliptical shape limits the fetch associated with northerly and southerly winds. The open ocean, with its larger area and essentially infinite boundary for wind fetch growth, tends to induce much lower frequencies of microseisms. Ocean wave activity may be more complex. The relationship between wave growth and variations in LFM peak frequency requires further examination to enhance future wave monitoring applications in the oceans.

The strain amplitudes measured by DAS can vary due to local environmental factors and cable configurations [58], e.g., how well the cable is coupled with the seabed, the cable declination with the topography, and the properties of the fiber cladding. These variations denote that the strain measurements may differ across different telecommunication infrastructures or even along different segments of the same cable. Therefore, local adjustments are required to accurately relate the amplitude measurements to actual wave conditions [48]. However, the peak frequency of LFMs tends to remain stable, making it a useful indicator for monitoring waves in areas where strong microseisms are detectable. The DAS technique provides valuable insights into wave dynamics and allows for continuous, real-time monitoring, even during severe weather conditions. Such high-resolution observations may constrain initial conditions for meteorological and ocean models, aiding in coastal hazard assessment, the understanding of wind-wave-driven ecosystems, and wave energy development.

4. Data and Methods

4.1 Experiment site and DAS settings

We analyzed DAS data acquired from the Crosslake fiber-optic telecommunication cable between Toronto and Buffalo (Fig. 1a). An Aragon Photonics interrogator, with chirped-pulse technology [59], was installed in Toronto during this ten-month experiment to measure continuous strain variations at a 200-Hz sampling rate, with several brief interruptions between July and September due to technical maintenance. The strains were measured along the first 50 km of the cable using a 10-m gauge length. The initial ~7 km of the cable (the first 701 channels) are underground on land, extending from Toronto’s city center to the shoreline. The remaining ~43 km segment, with an approximate azimuth of 130 degrees, is generally buried in sediments about 0.3 m beneath the lake floor. Along the location of the underwater cable (Fig. 1b, c), the lake bottom is at water depths <20 m for the first 3-km underwater cable (channels 702-1000). The water depths increase notably from 20 to 100 m within 6 km of the cable (channels 1001-1600) and then gradually increase to ~140 m between distances of 9 and 25.4 km from the shoreline. After that, the water depths decrease gently, with a mean slope gradient of 0.2 degrees, from ~140 to 110 m until the end of the measured channel at the distance of ~43 km to the shoreline of Toronto. Here, we focus on the data from 24 km of the cable between 9 and 33 km from the shoreline (channels 1600-4000), which has fewer turbulent disturbances.

4.2 DAS and environmental data processing

The 200-Hz continuous strain from the DAS interrogator was output every 10 min. To obtain 36-h waveforms for every event, we removed laser noises from the raw strain data using an in-house code from Aragon Photonics, sequentially connected the 10-min data to 36-h continuous records, and down-sampled the data to a 20-Hz sampling rate. In addition to data in the time domain, we analyzed wave activity using microseism variations in the frequency domain. We applied Fourier transform to the laser-denoised data from the 10-min outputs, averaged and integrated PSDs between 1 and 4 Hz for the HFMs, and searched for peak frequency and its PSD between 0.2 and 1 Hz for the LFMs, resulting in 10-min intervals of DAS spectral time series for further analysis.

To characterize sources of the DAS-detected microseisms from environmental data, we used observational and model weather and ocean data from the National Oceanic and Atmospheric Administration (NOAA). The observational weather data at Station Olcott are recorded at 10-min intervals by the Great Lakes Observing System. Meanwhile, water level data are collected at 6-min intervals by NOAA’s National Water Level Observation Network. The model data with hourly outputs come from the NOAA’s National Centers for Environmental

Prediction (NCEP) Great Lakes Operational Wave Model, whose partial outputs are also archived at NOAA's Great Lakes Environmental Research Laboratory [52, 53, 54]. The WW3 model for the Great Lakes applies the unstructured grid framework [55], which enables efficient computations for higher spatial resolution simulations of nearshore regions. We interpolated the unstructured data to a structured grid with an approximate spacing of 2 × 2 km to facilitate easier data processing.

4.3 Wind variability computation

To investigate the HFMs induced by wind-wave interactions, we calculated wind variability (V_{wf}) using the NDFD data, which was utilized to force WW3. Since wind drives waves at the surface of water and the wave motion is usually delayed relative to the wind motion, the wave motions at the current time step can be treated as the wind field at the previous time step. Here, we defined the wind variability as the spatial and temporal changes in the wind field that induce wind-wave interactions. To obtain the time series of wind variability, we calculated the time difference in wind speed for the east-west and north-south components ($\Delta u = u_{t2} - u_{t1}$ and $\Delta v = v_{t2} - v_{t1}$, respectively), where $t1$ and $t2$ represent the wind speed at the previous and current time steps, and then took the vector sum of the wind speed differences on the two horizontal components $V_{wf} = (\Delta u^2 + \Delta v^2)^{\frac{1}{2}}$.

4.4 JONSWAP spectrum and empirical wave growth factor

The JONSWAP spectrum [36] is an empirical model that describes how surface wave energy is distributed across different frequencies while the seas are still developing. In such conditions, waves can continue to grow through non-linear wave-wave interactions. To account for these non-linear interactions on wave development, the JONSWAP spectrum includes an extra peak enhancement factor and is represented by the following equation:

$$S(f) = \frac{\alpha g^2}{(2\pi f)^5} \cdot exp\left[-\frac{5}{4}\left(\frac{f_p}{f}\right)^4\right] \cdot \gamma^a \qquad (1)$$

where f is wave frequency in hertz, and g is the gravitational acceleration. The parameter $\alpha = 0.076\left(\frac{{U_{10}}^2}{F \cdot g}\right)^{0.22}$ is related to wind speed at 10 m above the surface (U_{10}) and wind fetch (F). The peak frequency (f_p) in the wave spectrum corresponds to the maximum energy and is defined by $f_p = \frac{22}{2\pi}\left(\frac{g^2}{U_{10} \cdot F}\right)^{\frac{1}{3}}$. The extra peak enhancement factor γ^a includes the constant $\gamma = 3.3$ with $a = exp\left[-\frac{(f-f_p)^2}{2\sigma^2 {f_p}^2}\right]$. The parameter σ describes the width of the spectrum, taking a value of 0.07 for $f \le f_p$ and 0.09 for $f > f_p$.

From the above functions, the peak frequency (f_p) in the wave spectrum, identifying the dominant wave period, refers to the combined influence of wind speed and wind fetch. Those variations reveal the processes of wave growth and development. Since we lack co-located wind observations with the DAS array, we calculate the $U_{10} \times F = g^2\left(\frac{22}{2\pi f_p}\right)^3$ using the peak frequency (f_p) picked in the LFM spectrum every 10 min of the DAS data and define it as the ‘empirical wave growth factor’ to analyze the spatial and temporal wave evolution in Lake Ontario during the selected events.

4.5 Wind fetch and theoretical wave growth factor estimation from the NDFD and WW3

We used the NDFD and WW3 data to estimate the theoretical wind fetch by the definition of effective fetch based on the Shore Protection Manual [56]. The effective fetch (F_e) averages nine radial fetch distances at 3-degree increments around the main wind direction, resulting in a sector area within a total 24-degree included angle centered at the referenced point. The effective fetch is defined by the following equation:

$$F_e = \frac{\sum_{i=1}^{i=9} F_i \cos^2\theta_i}{\sum_{i=1}^{i=9} \cos\theta_i} \qquad (2)$$

where F_i is each radial fetch and θ_i is the angle between the azimuths of the radial fetch and the center fetch along the wind direction. The effective fetch, which uses multiple fetch paths, is more consistent with observed wave conditions than the strict single fetch. These conditions include spatial wave variability, wave energy diminishment with distance, and geographical obstacles such as coastlines, islands, and underwater ridges [60]. By utilizing effective fetch estimation, these circumstances can be adjusted to achieve more accurate predictions of wave height and period.

Here, the array center at Channel 2835 was used as a reference point (Fig. 6a, Supplementary Fig. 5). The azimuth of the center fetch was defined based on the wind direction at the reference point. We accumulated the fetch distances from the reference point along the wind direction if the difference between the wind and wave directions was less than 24 degrees or if the fetch reached the shoreline. The other eight radial fetches were estimated using the same method but different azimuths. We estimated the effective fetch at each full hour of the NDFD and WW3 data and obtained the effective fetch variations for the entire month of January.

To calculate variations in the theoretical wave growth factor for discriminating the impact of wind speed and wind fetch on wave development, we multiplied the time series of effective fetch by the time series of height-corrected wind speed from near-surface wind in NDFD data. To correspond to the wind variables defined in the empirical functions of the JONSWAP spectrum, we converted the NDFD wind speed near the surface (U, approximately $h \approx 1$ m) to that at 10 m above the surface (U_{10}) using a wind profile power law relationship [61, 62], $U_{10} =$

$U\left(\frac{h_{10}}{h}\right)^{\alpha}$, where the coefficient $\alpha = 0.11$ was applied for the surface of water. Wind speed decreases exponentially toward the surface in the lower atmosphere due to frictional forces, which vary depending on surface materials. We used the theoretical wave growth factor variations as references to compare the empirical wave growth factor variations and examined if the DAS-detected LFM peak frequency variations relate to wave evolution.

Data availability

We used weather data from the Great Lakes Observing System, which can be accessed through the NOAA's National Data Buoy Center at https://www.ndbc.noaa.gov/. Water level collected by the NOAA's National Water Level Observation Network is available at https://tidesandcurrents.noaa.gov/. The wind field data from the National Digital Forecast Database, used to force the Great Lakes Operational Wave Model based on WAVEWATCH III, as well as the wave data, can be found on the Great Lakes Coastal Forecasting System website at https://www.glerl.noaa.gov/emf/waves/WW3/. The Great Lakes bathymetry data used in this paper [63, 64] are available from the National Centers for Environmental Information website at https://www.ncei.noaa.gov/products/great-lakes-bathymetry/. The weather, water level, model data, and 10-Hz DAS data from channels 2435, 2835, and 3235 used in the moderate wind and winter storm event analyses are available in a public data repository [65]. The complete DAS dataset is available from the corresponding author upon request.

References

1. Meucci, A., Young, I. R., Hemer, M., Kirezci, E. & Ranasinghe, R. Projected 21st century changes in extreme wind-wave events. *Sci. Adv.* **6**, eaaz7295 (2020).

2. Jabbari, A., Ackerman, J. D., Boegman, L. & Zhao, Y. Increases in Great Lake winds and extreme events facilitate interbasin coupling and reduce water quality in Lake Erie. *Sci. Rep.* **11**, 5733 (2021).

3. Sverdrup, H. U., & Munk, W. H. Empirical and theoretical relations between wind, sea and swell. *Trans. Amer. Geophys. Union* **27**, 823–827 (1946).

4. Charnock, H. Wind stress on a water surface. *Q. J. R. Meteorol. Soc.* **81**, 639–640 (1955).

5. Wu, J. Wind stress and surface roughness at air-sea interface, *J. Geophys. Res.* **74**, 444–455 (1969).

6. Miles, J. On the generation of surface waves by shear flows. *J. Fluid Mech.* **3**, 185–204 (1957).

7. Phillips, O. On the generation of waves by turbulent wind. *J. Fluid Mech.* **2**, 417–445 (1957).

8. Hasselmann, K. On the non-linear energy transfer in a gravity wave spectrum, 1, General theory. *J. Fluid Mech.* **12**, 481–500 (1962).

9. Barber, N. F., & Ursell, F. The generation and propagation of ocean waves and swell. I: Wave periods and velocities. *Philos. Trans. R. Soc. A* **24**, 527–560 (1948).

10. Snodgrass, F. E., Groves, G. W., Hasselmann, K. F. et al. Propagation of ocean swell across the Pacific, *Philos. Trans. R. Soc. London A* **259**, 431–497 (1966).

11. Rhie, J. & Romanowicz, B. Excitation of Earth's continuous free oscillations by atmosphere–ocean–seafloor coupling. *Nature* **431**, 552–556 (2004).

12. Bromirski, P. D., Duennebier, F. K. & Stephen, R. A. Mid-ocean microseisms. *Geochem. Geophys. Geosyst.* **6**, Q04009 (2005).

13. Hasselmann, K. A statistical analysis of the generation of microseisms. *Rev. Geophys.* **1**(2), 177–210 (1963).

14. Ardhuin, F., Gualtieri, L. & Stutzmann, E. How ocean waves rock the Earth: Two mechanisms explain microseisms with periods 3 to 300 s. *Geophys. Res. Lett.* **42**, 765–772 (2015).

15. Babcock, J. M., Kirkendall, B. A. & Orcutt, J. A. Relationships between ocean bottom noise and the environment. *Bull. Seismol. Soc. Am.* **84**(6), 1991–2007 (1994).

16. Bromirski, P. D., Flick, R. E. & Graham, N. Ocean wave height determined from inland seismometer data: Implications for investigating wave climate changes in the NE Pacific. *J. Geophys. Res.* **104**(C9), 20753–20766 (1999).

17. Chi, W.-C., Chen, W.-J., Kuo, B.-Y. & Dolenc D. Seismic monitoring of western Pacific typhoons. *Mar. Geophys. Res.* **31**(4), 239–251 (2010).

18. Davy, C., Barruol, G., Fontaine, F. R., Sigloch, K. & Stutzmann, E. Tracking major storms from microseismic and hydroacoustic observations on the seafloor. *Geophys. Res. Lett.* **41**, 8825–8831 (2014).

19. Lin, J., Ji, C., Ying, C. & Xu, W. Tropical cyclone wind speed inversion using seafloor Rayleigh-wave microseisms. *IEEE J. Ocean. Eng.* **50**(1), 73–83 (2025).

20. Longuet-Higgins, M. & Stewart, R. Radiation stress and mass transport in gravity waves, with application to 'surf beats'. *J. Fluid Mech.* **13**, 481–504 (1962).

21. Ardhuin, F., Stutzmann, E., Schimmel, M. & Mangeney, A. Ocean wave sources of seismic noise. *J. Geophys. Res.* **116**, C09004 (2011).

22. Haubrich, R. A. & McCamy, K. Microseisms: Coastal and pelagic sources. *Rev. Geophys.* **7**, 539–571 (1969).

23. Juretzek, C. & Hadziioannou, C. Where do ocean microseisms come from? A study of Love-to-Rayleigh wave ratios. *J. Geophys. Res.: Solid Earth* **121**, 6741–6756 (2016).

24. Jensen, F. B. & Schmidt, H. Shear properties of ocean sediments determined from numerical modeling of Scholte wave data. In: Akal, T., Berkson, J. M. (eds) *Ocean Seismo-Acoustics* (NATO Conf. Ser., **16**. Springer, Boston, MA., 1986).

25. Bromirski, P. D. & Duennebier, F. K. The near-coastal microseism spectrum: Spatial and temporal wave climate relationships. *J. Geophys. Res.* **107**(B8), 2166 (2002)

26. Longuet-Higgins, M. S. A theory of the origin of microseisms. *Philos. Trans. R. Soc.* A **243**, 1–35 (1950).

27. Smalls, P. T., Sohn, R. A., & Collins, J. A. Lake-bottom seismograph observations of microseisms in Yellowstone Lake. *Seismol. Res. Lett.* **90**(3), 1200–1208 (2019).

28. Farrell, J., Koper, K. D. & Sohn, R. A. The relationship between wind, waves, bathymetry, and microseisms in Yellowstone Lake, Yellowstone National Park. *J. Geophys. Res.: Solid Earth* **128**, e2022JB025943 (2023).

29. Kerman, B. R. & Mereu, R. F. Wind-induced microseisms from Lake Ontario. *Atmos. Ocean*, **31**(4), 501–516 (1993).

30. Anthony, R. E., Ringler, A. T. & Wilson, D. C. The widespread influence of Great Lakes microseisms across the Midwestern United States revealed by the 2014 polar vortex. *Geophys. Res. Lett.* **45**, 3436–3444 (2018).

31. Kerman, B. R., Mereu, R. F. & Roy, D. Wind-induced microseisms from large lakes. *Sea Surface Sound '94*, 143–156 (1995).

32. Xu, Y., Koper, K. D. & Burlacu, R. Lakes as a source of short-period (0.5–2 s) microseisms. *J. Geophys. Res.: Solid Earth* **122**, 8241–8256 (2017).

33. Carchedi, C. J. W., Gaherty, J. B., Webb, S. C. & Shillington, D. J. Investigating Short-Period Lake-Generated Microseisms Using a Broadband Array of Onshore and Lake-Bottom Seismometers. *Seismol. Res. Lett.* **93**(3), 1585–1600 (2022).

34. Webb, S. C. The equilibrium oceanic microseism spectrum. *J. Acoust. Soc. Am.* **92**, 2141–2158 (1992).

35. Pierson Jr., W. J. & Moskowitz, L. A proposed spectral form for fully developed wind seas based on the similarity theory of S. A. Kitaigorodskii. *J. Geophys. Res.* 69(24), 5181–5190 (1964).

36. Hasselmann, K., Barnett, T., Bouws, E. et al. Measurements of wind-wave growth and swell decay during the joint North Sea wave project (JONSWAP). *Ergänzugsh. Dtsch. Hydrogr. Z.* **12A**. (1973).

37. Forristall, G. Z. Measurements of a saturated range in ocean wave spectra. *J. Geophys. Res.* **86**(C9), 8075–8084 (1981).

38. Voermans, J. J., Smit, P. B., Janssen, T. & Babanin, A. V. Estimating wind speed and direction using wave spectra. *J. Geophys. Res.: Oceans* **125**, e2019JC015717 (2020).

39. Williams, E. F., Fernández-Ruiz, M.R., Magalhaes, R. et al. Distributed sensing of microseisms and teleseisms with submarine dark fibers. *Nat. Commun.* **10**, 5778 (2019).

40. Guerin, G., Rivet, D., van den Ende, M. P. A. et al. Quantifying microseismic noise generation from coastal reflection of gravity waves recorded by seafloor DAS. *Geophys. J. Int.* **231**(1), 394–407 (2022).

41. Xiao, H., Spica, Z. J., Li, J. & Zhan, Z. Detection of earthquake infragravity and tsunami waves with underwater distributed acoustic sensing. *Geophys. Res. Lett.* **51**, e2023GL106767 (2024).

42. Williams, E. F., Zhan, Z., Martins, H. F. et al. Surface gravity wave interferometry and ocean current monitoring with ocean-bottom DAS. *J. Geophys. Res.: Oceans* **127**, e2021JC018375 (2022).

43. Mata Flores, D., Sladen, A., Ampuero, J.-P., Mercerat, E. D. & Rivet, D. Monitoring deep Sea currents with seafloor distributed acoustic sensing. *Earth Space Sci.* **10**, e2022EA002723 (2023).

44. Lin, J., Fang, S., He, R. et al. Monitoring ocean currents during the passage of Typhoon Muifa using optical-fiber distributed acoustic sensing. *Nat. Commun.* **15**, 1111 (2024).

45. Pelaez Quiñones, J. D., Sladen, A., Ponte, A. et al. High resolution seafloor thermometry for internal wave and upwelling monitoring using Distributed Acoustic Sensing. *Sci. Rep.* **13**, 17459 (2023).

46. Xiao, H., Tanimoto, T., Spica, Z. J. et al. Locating the precise sources of high-frequency microseisms using distributed acoustic sensing. *Geophys. Res. Lett.* **49**, e2022GL099292 (2022).

47. Spica, Z. J., Nishida, K., Akuhara, T. et al. Marine sediment characterized by ocean-bottom fiber-optic seismology. *Geophys. Res. Lett.* **47**, e2020GL088360 (2020).

48. Meulé, S., Pelaez-Quiñones, J., Bouchette, F. et al. Reconstruction of nearshore surface gravity wave heights from distributed acoustic sensing data. *Earth Space Sci.* **11**, e2024EA003589 (2024).

49. Lindsey, N. J., Rademacher, H. & Ajo-Franklin, J. B. On the broadband instrument response of fiber-optic DAS arrays. *J. Geophys. Res.: Solid Earth* **125**, e2019JB018145 (2020).

50. Lindsey, N. J. & Martin, E. R. Fiber-optic seismology. *Annu. Rev. Earth Planet. Sci.* **49**, 309–336 (2021).

51. Glover, H. E., Wengrove, M. E. & Holman, R. Measuring hydrodynamics and exploring nearshore processes using distributed sensing of fiber-optic cable strain. *Coast. Eng.* **190**, 104487 (2024).

52. Tolman, H. L., Balasubramaniyan, B., Burroughs, L. D. et al. Development and implementation of wind-generated ocean surface wave models at NCEP. *Wea. Forecasting*, **17**(2), 311–333 (2002).

53. The WAVEWATCH III Development Group (WW3DG). User manual and system documentation of WAVEWATCH III version 6.07.1. Tech. Note 333. *NOAA/NWS/NCEP/MMAB*, 465 (2019).

54. Alves, J.-H., Tolman, H., Roland, A. et al. NOAA's great lakes wave prediction system: A successful framework for accelerating the transition of innovations to operations. *Bull. Am. Meteorol. Soc.* **104**(4), E837–E850 (2023).

55. Abdolali, A., Banihashemi, S., Alves, J. H. et al. Great Lakes wave forecast system on high-resolution unstructured meshes. *Geosci. Model Dev.* **17**, 1023–1039 (2024).

56. U.S. Army Corps of Engineers (USACE). Shore Protection Manual. Coastal Engineering Research Center: Fort Belvoir, Virginia, (1984).

57. Young, I. R., & Verhagen, L. A. The growth of fetch limited waves in water of finite depth. 1. Total energy and peak frequency. *Coastal Eng.* **29**(1–2), 47–78 (1996).

58. Reinsch, T., Thurley, T. & Jousset, P. On the coupling of a fiber optic cable used for distributed acoustic/vibration sensing applications—a theoretical consideration. *Meas. Sci. Technology* **28**, 12 (2017).

59. Magalhães, R., Neves, T., Scherino, L., Martin-Lopez, S. & Martins, H. F. Reaching long-term stability in CP-ϕOTDR. *J. Lightwave Technol.* **40**, 3916–3922 (2022).

60. Mason, L., Riseng, C., Layman, A. et al. Effective fetch and relative exposure index maps for the Laurentian Great Lakes. *Sci Data* **5**, 180295 (2018).

61. Counihan J. Adiabatic atmospheric boundary layers: A review and analysis of data from the period 1880–1972. *Atmos. Environ.* **9**, 871–905 (1975).

62. Touma, J. S. Dependence of the wind profile power law on stability for various locations. *J. Air Pollut. Control Assoc.* **27**, 863–866 (1977).

63. National Geophysical Data Center. Bathymetry of Lake Ontario. NOAA National Centers for Environmental Information. https://doi.org/10.7289/V56H4FBH (1999).

64. National Geophysical Data Center. Bathymetry of Lake Erie and Lake St. Clair. NOAA National Centers for Environmental Information. https://doi.org/10.7289/V5KS6PHK (1999).

65. Yang, C.-F., Spica, Z., Fujisaki-Manome, A., & Miao, Y. Dataset for ‘Fiber-optic Observations Capture Wind Wave Evolution in Lake Ontario.” Data sets. Zenodo. https://doi.org/10.5281/zenodo.17410006 (2026).

Acknowledgements

We thank Crosslake Fibre for their assistance during the experiment. We thank Yang Li, Jing Ci Neo, and Marcelle Collares for supporting the installation and retrieval of the DAS integrator. We thank Bryan Mroczka and Dan Titze for accessing the wind and wave data archived at NOAA Great Lakes Environmental Research Laboratory. We thank the editor and anonymous reviewers for their valuable comments and constructive suggestions. C.-F.Y. expresses gratitude to Dr. Wu-Cheng Chi for the valuable discussions and to the postdoctoral fellowship program at CIGLR for awarding the NOAA grant NA22OAR4320150. Y.M. was partially supported by the U.S. Geological Survey award G23AP00498. This research (CIGLR contribution number XXXX) was supported by the CIGLR Seed Funding under the same NOAA grant

NA22OAR4320150. Data was processed using ObsPy (version 1.4.0; URL: http://docs.obspy.org), NumPy (version 1.26.4; URL: https://numpy.org/), and SciPy (version 1.12.0; URL: https://scipy.org/). Maps and figures were plotted with Matplotlib graphic tool (version 3.4.3; URL: http://matplotlib.org) for Python (version 3.9.7).

Author contributions

C.-F.Y. initiated this study, performed the formal analysis, and led the writing of the manuscript. Z.S. conceived and initiated the project and secured funding. A.F.-M. processed the wave, wind, and bathymetry data. Y.M. processed the raw DAS data. All authors reviewed and commented on the manuscript.

Competing interests

The authors declare no competing interests.

Figure captions

Figure 1 Location of the Crosslake Distributed Acoustic Sensing (DAS) array and the National Oceanic and Atmospheric Administration (NOAA) weather station. (a) Map view of Lake Ontario. Red line marks the 50-km DAS array. Yellow triangle marks the observation station for weather and water level data. (b) Cross-section view of water depths along the array shows the channel distances to the shoreline of Toronto. Red and magenta stars mark channel 2835 at the center of the array and channel 3285 at the deepest water depth, respectively. (c) A 3D view shows the bathymetry where the array is located.

Figure 2 DAS data are compared to wind observations at Station Olcott during the moderate wind event (from 12 UTC on May 16 to 00 UTC on May 18, 2023) and the winter storm event (from 12 UTC on January 9 to 00 UTC on January 11, 2024). (a) The DAS strain spectrogram at the center of the array (channel 2835) is compared with time series of wind speed and direction during the moderate wind event. (b) Filtered and normalized strain variations in the microseismic frequency band from channels 2000 to 4000 of the array (in intervals of 10 channels) are shown for the period marked between the dashed lines in (a). The normalized scales are different for two events. Darker areas indicate the higher amplitudes of strain. The channels are located 13-33 km from the shoreline of Toronto, and the water depths are shown on the right Y axis. A star on the water-depth scale marks the deepest location at channel 3285, about 25.8 km from Toronto's shoreline. Blue arrows on top represent the wind field at 6-min intervals. (c) and (d) are the same as (a) and (b), respectively, but during the winter storm event.

Figure 3 Averaged spectrum of strain rate from the DAS array between channels 1600 and 4000 with 10-channel intervals for (a) the moderate wind event and (b) the winter storm event. Different line colors mark the array's distance to the shoreline of Toronto. Channels 1600-3000 shown on the left panel are located on the north slope near Toronto, while channels 3000-4000 shown on the right panel are located on the south slope near Lockport. Blue label on the color bar marks the corresponding depths of the distance to the shoreline of Toronto. A star marked with a depth of 139 m at ~25 km is the deepest depth of the array (see Fig. 1b).

Figure 4 DAS-detected high-frequency microseisms (HFMs) are compared to wind data from the National Digital Forecast Database (NDFD), wave data from the WAVEWATCH III, as well as wind and water levels observed at Station Olcott during the (a and b) moderate wind and (c and d) winter storm events. (a) and (c) show map views of NDFD wind variability (color shading) and areas where the wind-wave direction discrepancy exceeds 24° (gray overlay). Solid gray line marks the wavefront. Behind the wavefront, the wind and wave have a consistent moving direction. Red and black arrows in (a) and (c) represent the wind field at the time displayed on the title and at its prior time step (one hour before the time on the title), respectively. Yellow triangle marks the location of Station Olcott. (b) and (d) show power spectral densities (PSDs, colored dot) averaged in the HFM frequency band on DAS channels 2435, 2835, and 3235, as well as the wind variability (red line with cross marks) calculated by NDFD data. Light red line presents the time shifted wind variability fitting the maximum PSD of HFM. The bottom panel shows the wind variability and water level (blue line) variations at Station Olcott. Dashed red and blue lines mark the times of the highest wind variability and highest water level observed at Station Olcott, respectively.

Figure 5 Spatiotemporal variations of DAS-detected microseisms are compared to wind and wave data from the National Digital Forecast Database (NDFD) and WAVEWATCH III (WW3), respectively. Four panels from top to bottom depict (a) spatiotemporal variations of WW3 significant wave height, (b) empirical wave growth factors, (c) energy at the peak frequency of low-frequency microseisms, and (d) integrated energy of high-frequency microseisms between 1 and 4 Hz, respectively, during the moderate wind event. Blue arrows are NDFD wind fields at the array center position (channel 2835). Red or black markers shown on each panel are the corresponding temporal variations at the array center position, and their relative amplitudes are scaled by the vertical arrows on the left. (e), (f), (g), and (h) are the same as (a), (b), (c), and (d), respectively, but during the winter storm event.

Figure 6 DAS-detected low-frequency microseisms (LFMs) are compared to wind data from the National Digital Forecast Database and wave data from the WAVEWATCH III in January 2024. (a) Time series of LFM peak frequency, empirical wave factor, and energy of LFM peak frequency from the DAS data are compared to time series of wind speed, wind direction, theoretical wave factor, wind fetch, and significant wave height at channel 2835 of the array center. Light yellow shading marks the storm period when two winter storms influence Lake Ontario. Light blue arrows indicate the local maximum wind fetch, which corresponds to the persistent easterly wind. (b) Time-shift-corrected DAS empirical wave factors against theoretical wave factors during the storm period shown in (a). The statistic presents the empirical wave factors between channels 2435 and 3235 with 200-channel intervals versus the theoretical wave factors from the corresponding locations. Color shading indicates the percentage of 538 data points during the storm period. Solid and dashed red lines are the linear regression to fit the wave factor distributions and their standard deviations. R is the Pearson correlation coefficient between two datasets. (c) the same as (b) but using 2400 data points during the entire month of January.

Figure 7 Illustration of a wind wave's entire life cycle, starting with high-frequency chaotic waves and ripples that gradually evolve into a low-frequency surface gravity wave during the winter storm event. The spectrogram in the top panel is the same as Fig. 2c but is overlaid with the wind field observed at Station Olcott. The bottom panel depicts a conceptual model of how a gravity wave generated by wind evolves over time, with various white curves referencing the microseismic spectrogram and wind field time series. During the period of intermittent winds, the ripples and chaotic waves (thin, small curves), which are the sources of high-frequency microseisms, are ubiquitous over the water surface due to wind- and wave-wave interactions. In the meantime, a low-amplitude wind-driven gravity wave (thick, faint curves) is propagating from the farther east. When the wind field turns to consistent southwesterly winds, the wind transfers energy into the water and bundles the chaotic waves, gradually forming a gravity wave (thick, intense curves), which is the source of low-frequency microseisms. As the winds continue to blow nearly in the same direction, the wind fetch increases, while the gravity wave grows to a lower frequency (longer period) and greater amplitude. Once the fetch reaches its maximum distance due to the limitation of the lake's shore boundary, the gravity wave starts to dissipate, and the fetch is slowly decreasing. This dynamic process indicates another path for the evolution between primary and secondary microseisms: secondary microseisms can be induced by the ripples and chaotic waves at the early stage of wind-wave development, occurring before primary microseisms. Dashed black line marks to distinguish two different wave-dominant periods.

Editorial summary:
Fiber-optic cables can be employed as seismic sensors to understand wind-wave activities in large water bodies, according to distributed acoustic sensing data from Lake Ontario.

Peer review information:
Communications Earth and Environment thanks the anonymous reviewers for their contribution to the peer review of this work. Primary Handling Editors: Jan Dettmer and Alice Drinkwater. A peer review file is available.

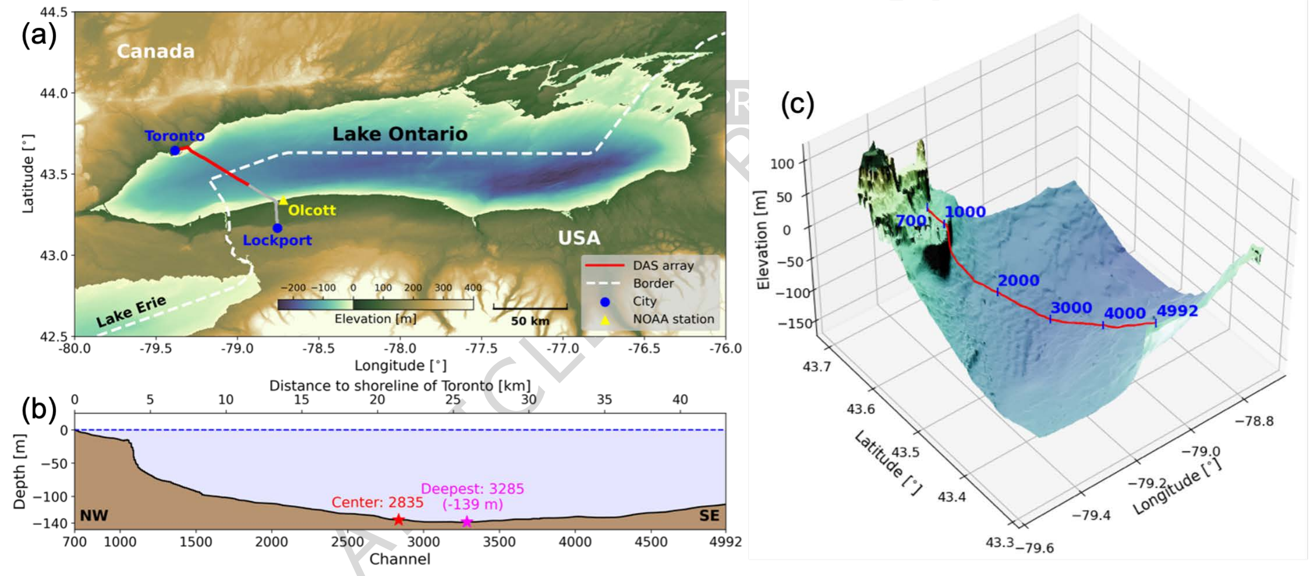
(a)
Canada
Lake Ontario
Toronto
Olcott
Lockport
USA
Lake Erie
DAS array
Border
City
NOAA station
Elevation [m]
50 km
Latitude [°]
Longitude [°]
(b)
Distance to shoreline of Toronto [km]
Depth [m]
NW
SE
Center: 2835
Deepest: 3285
(-139 m)
Channel
(c)
Elevation [m]
700
1000
2000
3000
4000
4992
Latitude [°]
Longitude [°]

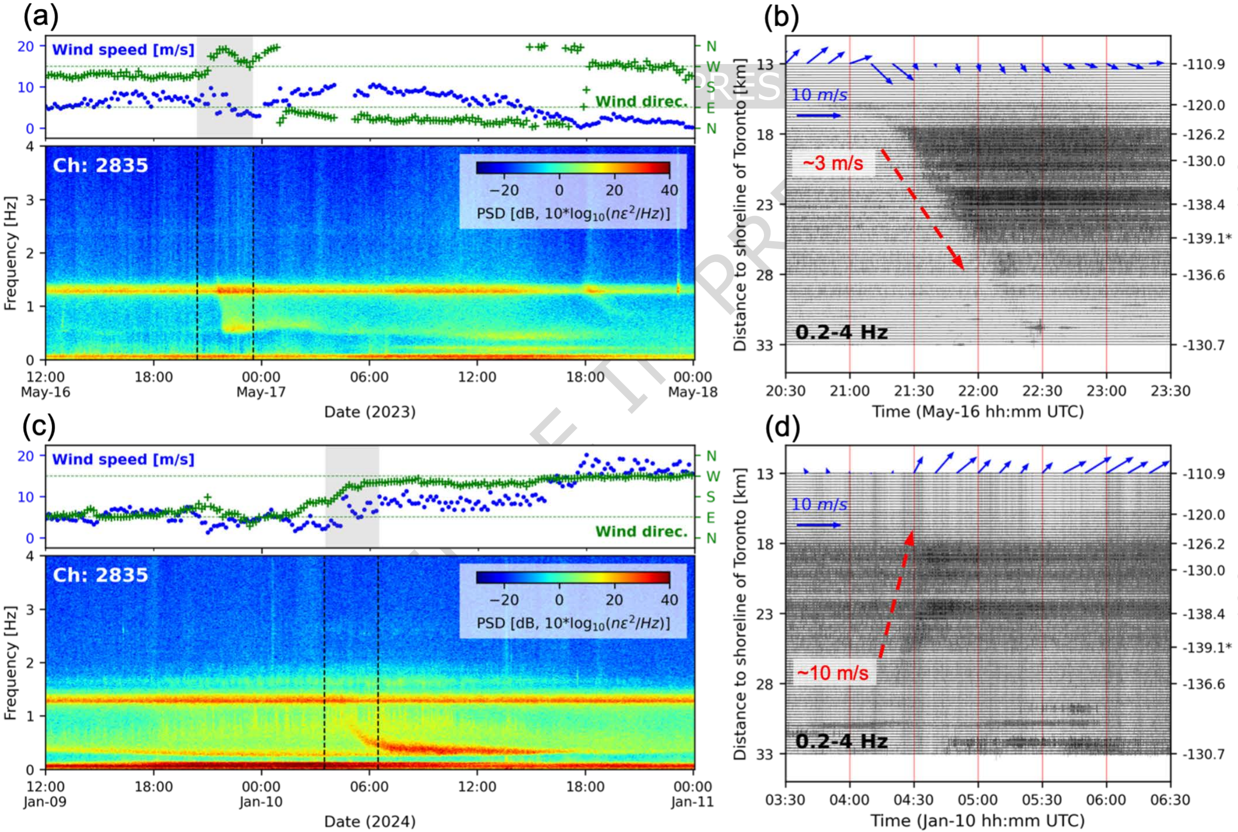
(a)
Wind speed [m/s]
Wind direc.
N
W
S
E
N
Ch: 2835
PSD [dB, 10*log10(nε2/Hz)]
Frequency [Hz]
12:00 May-16
18:00
00:00 May-17
06:00
12:00
18:00
00:00 May-18
Date (2023)
(b)
10 m/s
~3 m/s
0.2-4 Hz
Distance to shoreline of Toronto [km]
Depth [m]
-110.9
-120.0
-126.2
-130.0
-138.4
-139.1*
-136.6
-130.7
20:30
21:00
21:30
22:00
22:30
23:00
23:30
Time (May-16 hh:mm UTC)
(c)
Wind speed [m/s]
Wind direc.
Ch: 2835
PSD [dB, 10*log10(nε2/Hz)]
Frequency [Hz]
12:00 Jan-09
18:00
00:00 Jan-10
06:00
12:00
18:00
00:00 Jan-11
Date (2024)
(d)
10 m/s
~10 m/s
0.2-4 Hz
Distance to shoreline of Toronto [km]
Depth [m]
03:30
04:00
04:30
05:00
05:30
06:00
06:30
Time (Jan-10 hh:mm UTC)

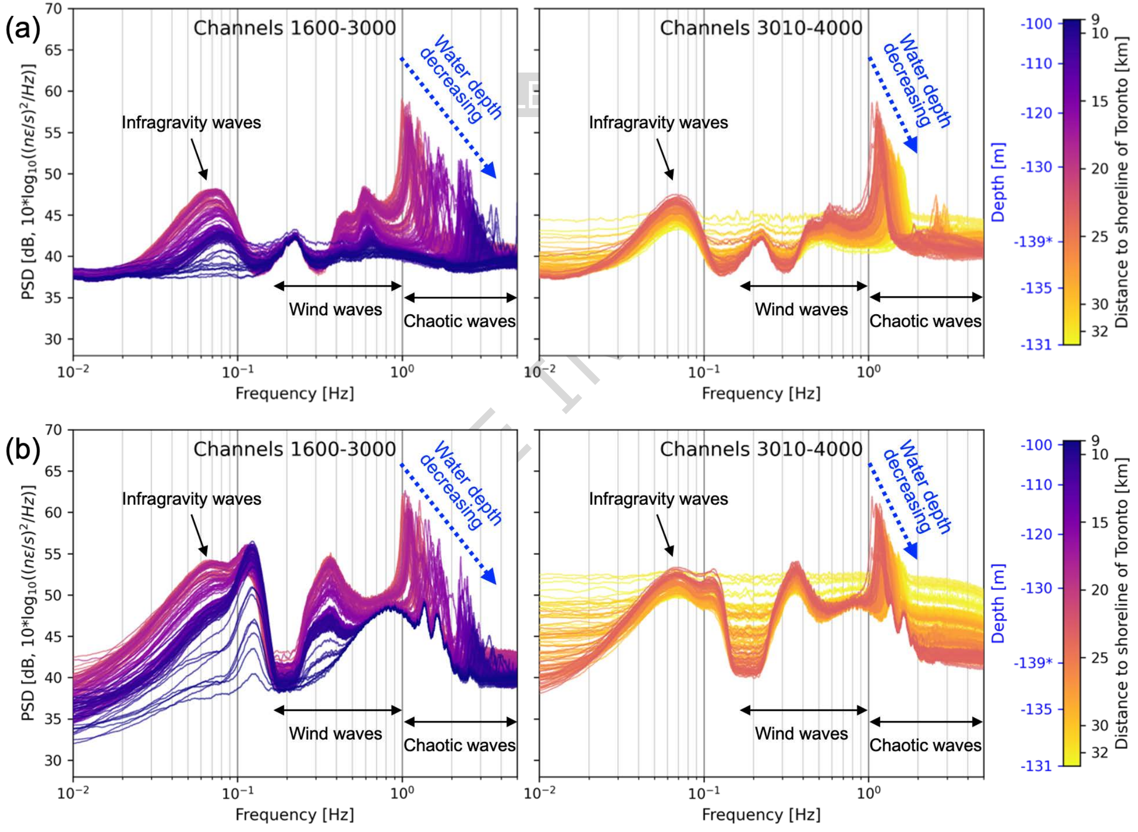
(a)
Channels 1600-3000
Channels 3010-4000
Infragravity waves
Water depth decreasing
Wind waves
Chaotic waves
PSD [dB, $10*\log_{10}((n\varepsilon/s)^2/Hz)$]
Frequency [Hz]
Depth [m]
Distance to shoreline of Toronto [km]
-100
-110
-120
-130
-139*
-135
-131
9
10
15
20
25
30
32
(b)
Channels 1600-3000
Channels 3010-4000
Infragravity waves
Water depth decreasing
Wind waves
Chaotic waves
PSD [dB, $10*\log_{10}((n\varepsilon/s)^2/Hz)$]
Frequency [Hz]
Depth [m]
Distance to shoreline of Toronto [km]

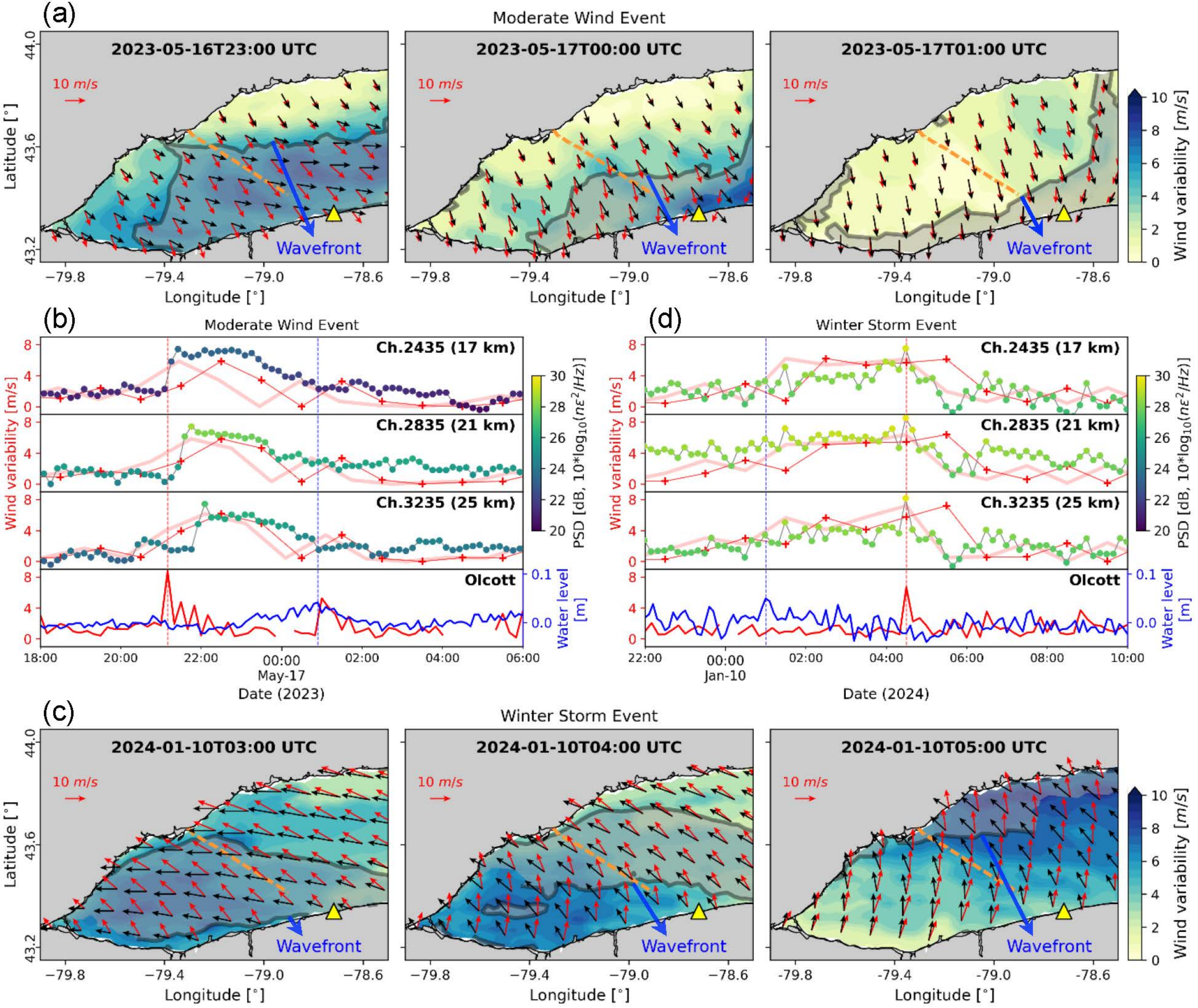

(a)
Moderate Wind Event
2023-05-16T23:00 UTC
2023-05-17T00:00 UTC
2023-05-17T01:00 UTC
10 m/s
Wavefront
Latitude [°]
Longitude [°]
Wind variability [m/s]
(b)
Moderate Wind Event
Ch.2435 (17 km)
Ch.2835 (21 km)
Ch.3235 (25 km)
Olcott
Wind variability [m/s]
Water level [m]
PSD [dB, 10*log10(nε²/Hz)]
May-17
Date (2023)
(d)
Winter Storm Event
Jan-10
Date (2024)
(c)
Winter Storm Event
2024-01-10T03:00 UTC
2024-01-10T04:00 UTC
2024-01-10T05:00 UTC

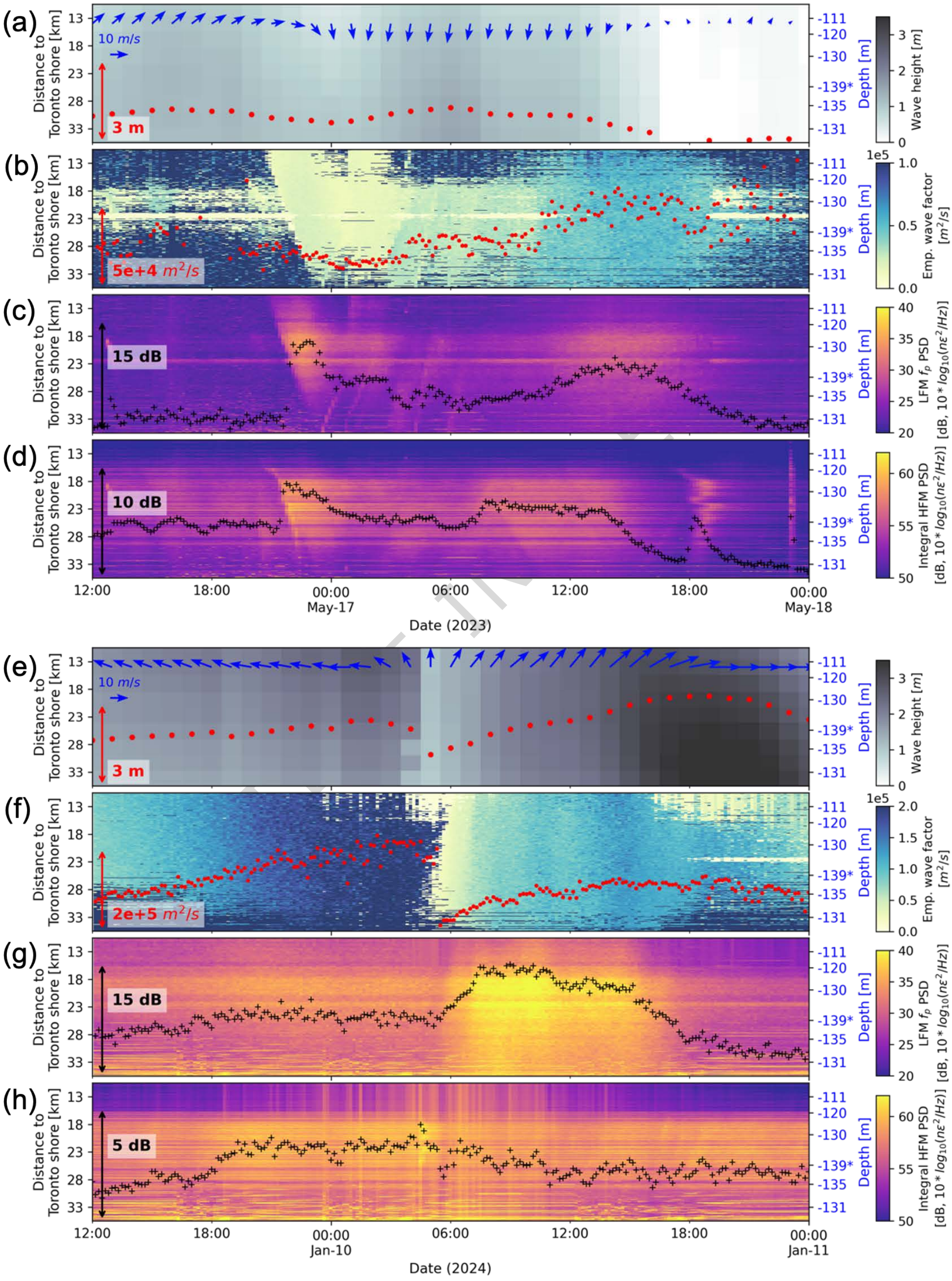

(a)
(b)
(c)
(d)
(e)
(f)
(g)
(h)
Distance to Toronto shore [km]
Depth [m]
10 m/s
3 m
5e+4 m^2/s
15 dB
10 dB
2e+5 m^2/s
5 dB
Wave height [m]
Emp. wave factor [m^2/s]
LFM f_p PSD [dB, $10*log_{10}(n\varepsilon^2/Hz)$]
Integral HFM PSD [dB, $10*log_{10}(n\varepsilon^2/Hz)$]
1e5
12:00
18:00
00:00
May-17
06:00
12:00
18:00
00:00
May-18
Date (2023)
Jan-10
Jan-11
Date (2024)

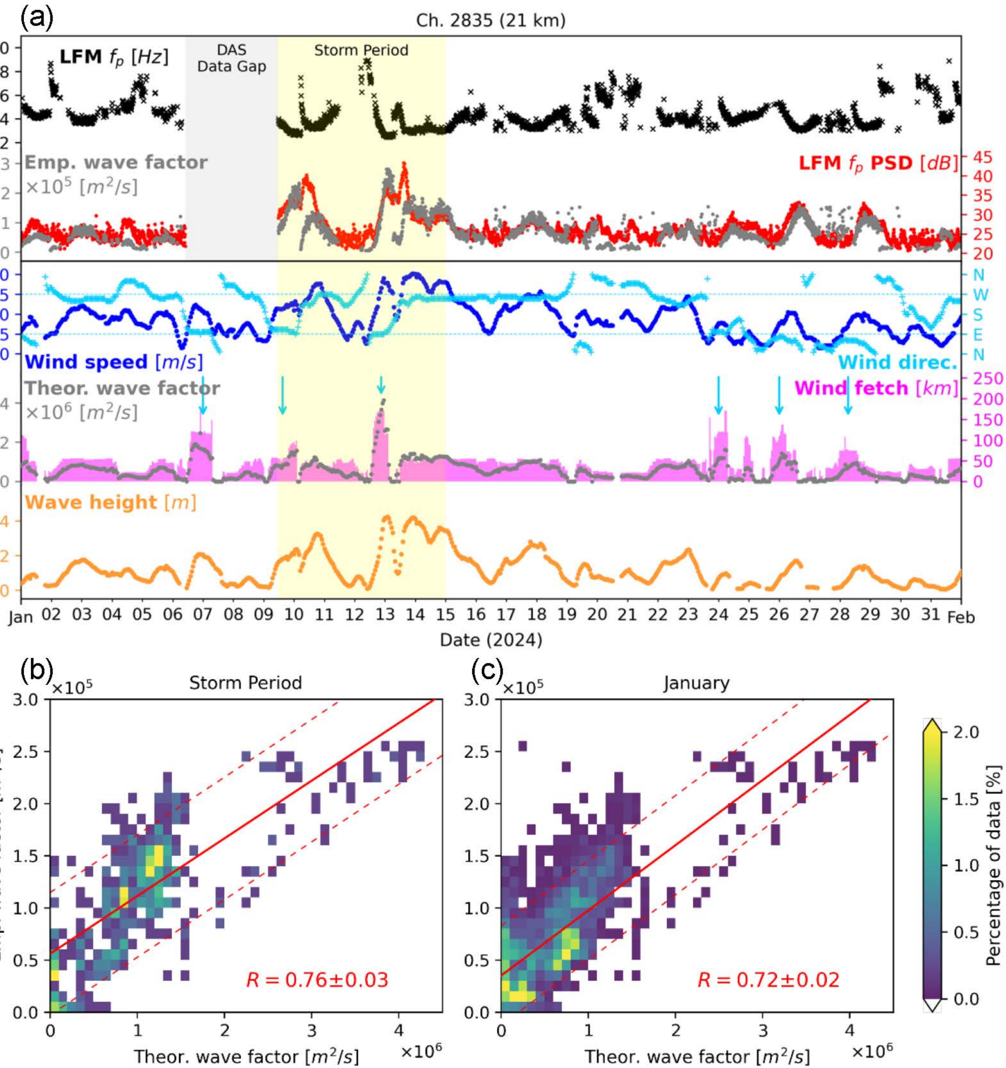
(a)
Ch. 2835 (21 km)
LFM f_p [Hz]
DAS Data Gap
Storm Period
Emp. wave factor ×10^5 [m^2/s]
LFM f_p PSD [dB]
Wind speed [m/s]
Wind direc.
Theor. wave factor ×10^6 [m^2/s]
Wind fetch [km]
Wave height [m]
Date (2024)
(b)
Storm Period
$R = 0.76 \pm 0.03$
(c)
January
$R = 0.72 \pm 0.02$
Emp. wave factor [m^2/s]
Theor. wave factor [m^2/s]
Percentage of data [%]

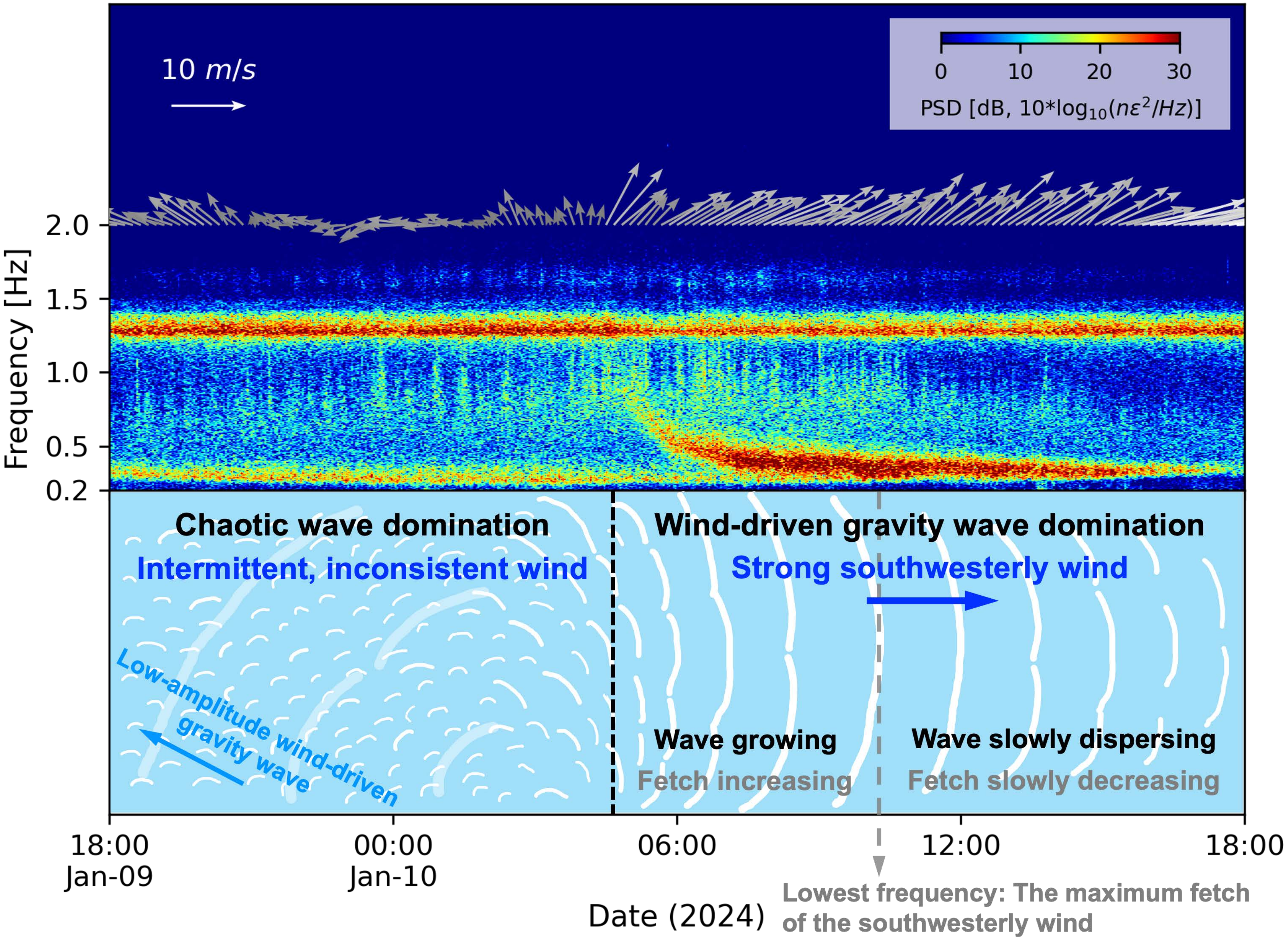
10 m/s
0
10
20
30
PSD [dB, 10*log10(nε²/Hz)]
Frequency [Hz]
2.0
1.5
1.0
0.5
0.2
Chaotic wave domination
Intermittent, inconsistent wind
Low-amplitude wind-driven gravity wave
Wind-driven gravity wave domination
Strong southwesterly wind
Wave growing
Fetch increasing
Wave slowly dispersing
Fetch slowly decreasing
18:00 Jan-09
00:00 Jan-10
06:00
12:00
18:00
Date (2024)
Lowest frequency: The maximum fetch of the southwesterly wind